Journal of Applied Fluid Mechanics, Vol. 12, No. 3, pp. 777-788, 2019.
Available online at www.jafmonline.net, ISSN 1735-3645, EISSN 1735-3645.
DOI: 10.29252/jafm.12.03.29302

Large-Eddy Simulation of a Laminar Separation Bubble

N. K. Singh

Department of Mechanical Engineering, National Institute of Technology, Kurukshetra, Haryana, 136119, India

†*Corresponding Author Email: nksinghfme@nitkkr.ac.in*

(Received June 23, 2018; accepted October 9, 2018)

ABSTRACT

Large-eddy simulation of a laminar separation bubble on a flat plate has been performed and compared with the data in the literature. Suitability of different subgrid-scale models has been examined for simulation of transition. Comparison of various parameters and three-dimensional visualization of instantaneous flow fields indicate that standard Smagorinsky model, being too dissipative, is not suitable for this kind of problem and fails to properly resolve transition. With the application of low Reynolds number correction and a reduced model constant, a good agreement with the dynamic model is obtained at a lower computational cost. Of the three SGS models investigated, dynamic model gives the most physically accurate description of transition. The simulations illustrate that the appearance of Λ-vortices, vortex stretching and break down of longitudinal streaks characterize the transition process. Low values of reverse flow make it clear that a convective instability is involved. It is concluded that the initial amplification of disturbances is due to Tollmien - Schlichting mechanism while the roll-up of the shear layer takes place due to Kelvin-Helmholtz instability. It is observed that the universal log-law profile is not reached by the velocity profiles even far downstream.

Keywords: Separation bubble; Large-eddy simulation; Smagorinsky model; Dynamic model.

NOMENCLATURE

C_f	skin friction coefficient	u_m	mean streamwise velocity
C_p	coefficient of pressure	U_∞	free stream velocity at inlet
C_S	smagorinsky model constant		
p	pressure	τ_w	wall shear stress
rms	root mean square		
$Re_{\delta^*_{in}}$	Reynolds number based on displacement thickness at inlet and free stream velocity	δ	boundary layer thickness
		δ^*	displacement thickness
Re_{lt}	Reynolds number based on transition length	δ^*_{in}	displacement thickness at inlet
Re_{θ_S}	Reynolds number based on the boundary layer momentum thickness at separation	$\boldsymbol{\theta}$	momentum thickness
		$\boldsymbol{\theta_s}$	momentum thickness at separation
u_τ	friction velocity	τ_{ij}	sub-grid scale tensor

1. INTRODUCTION

Laminar separation bubbles (Fig. 1) are usually found in low Reynolds number flows such as flows over airfoils or low-pressure (LP) turbine blades where the flow separates under steady flow conditions. The separated shear-layer undergoes transition as it is highly sensitive to perturbations near the point of separation. Non-linear breakdown of traveling waves is hypothesized to be the cause of transition (Dovgal *et al*. 1994). The flow is re-energized by the resultant turbulent layer and reattachment takes place to form a separation bubble (Horton, 1967; Roberts, 1980).

The ability to predict and control the formation of laminar separation bubble has great practical importance in many engineering flows. Still the knowledge of flow structures and mechanism of transition in the bubble region is incomplete (Jones *et al*., 2010). The receptivity of the bubble to the disturbances arising from different sources is only partly understood. The present study aims to

simulate the flow environment of a laminar separation bubble to look into the mechanism of transition, generation of large and small-scale eddies and their interactions.

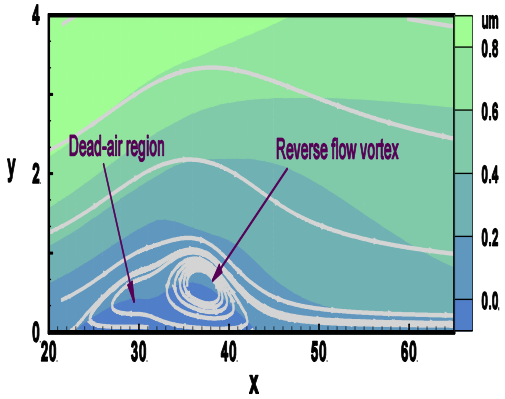

Fig. 1. Laminar separation bubble showing contours of u_m, streamlines (light coloured) and other features.

Early numerical work on laminar separation bubbles focused on the prediction of time-averaged structure and this trend remained unchanged up to early nineties. Since the beginning of nineties, a number of researchers used Navier-Stokes equation to resolve details of unsteady separation bubbles. Pauley *et al.* (1990) simulated unsteady structures in a rectangular channel without using a turbulence model. It was observed that the adverse pressure gradient caused periodic vortex shedding. Ripley and Pauley (1993) simulated the characteristics of separation found in experimental study of Gaster (1967). Allen and Riley (1995) describe an investigation into the flow properties associated with small two-dimensional separation bubbles, commonly found on the leading edge of airfoils. Lin and Pauley (1996) numerically investigated separation from an airfoil. According to them, the unsteadiness of shear layer is caused by a Kelvin-Helmholtz (*K-H*) instability.

The DNS of Alam and Sandham (2000) and Spalart and Strelets (2000) fully resolve the transition in a laminar separation bubble. It is inferred by Alam and Sandham (2000) that the Λ-vortex-induced breakdown causes the transition in the separated shear layer which then reattaches as turbulent flow. The turbulent layer then undergoes a slow recovery. Spalart and Strelets (2000) used suction in a channel flow to generate the adverse pressure gradient. However, they did not consider artificial forcing of disturbances upstream of separation. They discard the entry-region disturbances as the cause of transition and conclude that the transition process includes a wavering shear layer followed by *K-H* vortices, which instantly become three-dimensional. Yang and Voke (2001) predicted the characteristics of laminar separation bubble and transition at a change of surface curvature. Marxen *et al.* (2003) introduced 2-D disturbances upstream of separation using an oscillating wire and imposed 3-D disturbances using array of thin metal spacers. Their conclusion is that viscous *T-S* instability is the primary instability mechanism. Wissink and Rodi (2003) performed their DNS of separation bubble in the presence of oscillating flow. They conclude that a *K-H* instability, such as found in the laminar separation bubble simulation with steady inflow (Spalart and Strelets, 2000), causes the initial roll-up of the shear layer

Roberts and Yaras (2006) and McAuliffe and Yaras (2008) used a coarse DNS to examine transition in a separation bubble. Jones *et al.* (2010) investigated the flow around an airfoil using very low amplitude perturbations. They could not find any evidence of absolute instability. The interaction of mean flow and transition in a transitional separation bubble was investigated by Marxen and Rist (2010) while The interaction of different instability modes in the process of transition in a separation bubble was numerically investigated by Brinkerhoff and Yaras (2011).

It is evident from the above discussion that despite such a long history of research, the problem of transition in a laminar separation bubble is only partly understood and still demands attention. One of the principal objectives of this study is to resolve the physics of a laminar separation bubble by LES and to examine the effect of sub-grid models. Here, focus is on the applicability of Smagorinsky model against the dynamic model in predicting transition of the separated layer, coherent structures and turbulent eddies near and after reattachment. The receptivity of disturbances of the separated layer leading to transition and breakdown has also been discussed.

2. NUMERICAL FORMULATION

2.1 Governing Equations

The filtered mass and momentum equations, for an incompressible fluid flow in a Cartesian coordinate system, can be given as,

$$\frac{\partial \bar{u}_j}{\partial x_j} = 0 \tag{1}$$

$$\frac{\partial \bar{u}_i}{\partial t} + \frac{\partial}{\partial x_j}\left(\bar{u}_j \bar{u}_i\right) = -\frac{\partial \bar{p}}{\partial x_i} + \frac{1}{\mathrm{Re}_{\delta_{in}^*}} \nabla^2 \bar{u}_i - \frac{\partial \tau_{ij}}{\partial x_j} \tag{2}$$

Here, u_i and p denote velocity and pressure fields respectively while the overbar denotes the filtered variables The SGS tensor is calculated by Smagorinsky model (Smagorinsky, 1963) for two values of model coefficients C_s, 0.17 & 0.1 apart from the dynamic model proposed by Germano *et al.* (1991) and modified by Lilly (1992).

Schematic of the computational domain is shown in Fig. 2. The lengths are scaled with respect to δ_{in}^* and the velocities with respect to U_∞. Dimensions of the computational box are given in Table 1. It should be noted that Alam and Sandham (2000) had taken the same domain dimensions. The flow Reynolds number based on δ_{in}^* and U_∞ is 500.

Table 1 Dimensions of the computational box.

$L_x(\delta^*_{in})$	$L_y(\delta^*_{in})$	$L_z(\delta^*_{in})$
200	10	30

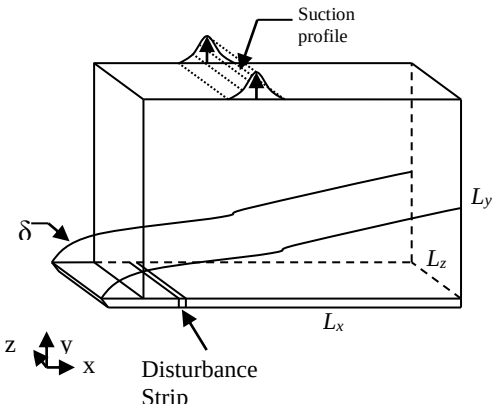

Fig. 2. Schematic of the computational domain.

2.2 Boundary Conditions

At the inlet, a Blasius velocity profile is specified for u corresponding to $Re_{\delta^*_{in}}$ = 500, while v =w =0.

A convective boundary condition (Orlanski, 1976) is imposed at the outlet, which can be written as

$$\frac{\partial u_i}{\partial t} + U_c \frac{\partial u_i}{\partial x_c} = 0 \tag{3}$$

Here, subscript c denotes the direction normal to the outflow boundary. U_c, the convective velocity is considered to be constant across the outflow boundary and is fixed at each time step by averaging the velocity normal to the boundary over a transverse plane.

On the lower boundary a no-slip condition is applied i.e. $u = v = w = 0$. At the upper boundary, u = 1.0 and $v = w = 0$ and a suction profile following the Gaussian distribution of the wall-normal velocity component has been specified. The expression of the suction-velocity distribution following Alam and Sandham (2000) is given by,

$$S(x) = a_s \exp[-b_s (x - c_s)^2] \tag{4}$$

The values of constants are given in the Table 2. Because of Gaussian distribution, the suction will be effective locally as shown in Fig. 2.

Table 2 Numerical parameters of suction and forcing profile

a_s	b_s	c_s	a_f	b_f	c_f	ω	β
0.15	0.02	25	30.08^{-3}	0.125	10	0.15	0.41

As naturally occurring disturbances are non-existent in numerical simulations, a disturbance strip applied upstream of separation triggers the transition of shear layer. The disturbance strip is applied to the normal velocity by the function given below, following Alam and Sandham (2000).

$$v'(x,z,t) = a_f \exp[-b_f (x - c_f)^2] \sin(\omega t) \sin(\beta z) \tag{5}$$

The constants a_f, b_f and c_f controlling the disturbance are given in Table 2. The flow is

assumed to be homogeneous in the spanwise direction; hence a periodic boundary condition is applied to all the velocity components in the spanwise direction.

2.3 Computational Details

The grid is slowly stretched in the wall-normal direction while the grid is uniform in the other two directions. In Table 3, a comparison of the grid spacing has been made with the simulations of Spalart (1988), Kim *et al*. (1987) and Alam and Sandham (2000). The wall shear stress varies along the streamwise direction and accordingly u_τ varies. Here, the wall units are calculated on the basis of u_τ at x = 170, where the boundary layer has relaxed to an approximate canonical layer. The wall units in other two directions are evaluated in a similar manner. The resolutions are compared in terms of Δx^+, Δy^+ and Δz^+ at y^+ = 9.0. Further, number of grid points within y^+= 9.0 (N) is tabulated to assess the near wall resolution.

Table 3 Comparison of the wall units

Case		Δx^+	Δy^+ at y^+ = 9	Δz^+	N
KMM		11.78	1.33	7.00	13
Spalart		20.00	-	6.70	10
Alam & Sandham		20.73	0.90	6.20	16
Present LES	160×64×32	31.18	1.24	23.4	8
	200×64×32	24.64	1.23	23.1	8
	200×64×64	24.38	1.21	11.25	8
	260×64×64	16.07	1.20	10.96	8
	260×96×64	16.14	0.72	11.21	13

To ensure grid independence, simulations were carried out using five levels of mesh, viz. 160×64×32, 200×64×32, 200×64×64, 260×64×64 and 260×96×64 cells in the x, y and z directions respectively. Variations of C_f for different grid levels are plotted in Fig. 3. It can be seen from Fig. 3 that the changes in evolution of C_f and bubble length are insignificant as the 200×64×64 grid is refined further. Hence, a mesh of 200×64×64 points is chosen here for subsequent calculations.

It should be noted that the near wall resolution at x = 170, where an attached turbulent layer appears, is $\Delta x^+ \approx$ 24, $\Delta y^+ \approx$ 1.0 and $\Delta z^+ \approx$ 11. Turbulent boundary layer simulations using a second-order accurate scheme roughly need $\Delta x^+ \approx$ 50, $\Delta y^+ \approx$ 1.0,

$\Delta z^+ \approx 20$ for a LES and $\Delta x^+ \approx 15$, $\Delta y^+ \approx 1.0$, $\Delta z^+ \approx 6$ for a DNS (Ovchinnikov *et al.*, 2006). However, the grid requirements are less established for resolution of transitional flow, which obviously demands more refined grid and may be problem dependent. Based on the previous work (Sarkar, 2007, 2008, 2009; Sarkar and Sarkar, 2009), it appears that the present mesh is capable of resolving transition. With the chosen grid, simulations are performed for the following cases,

(i) Smagorinsky model, C_s= 0.17

(ii) Smagorinsky model, C_s= 0.1

(iii) Dynamic model.

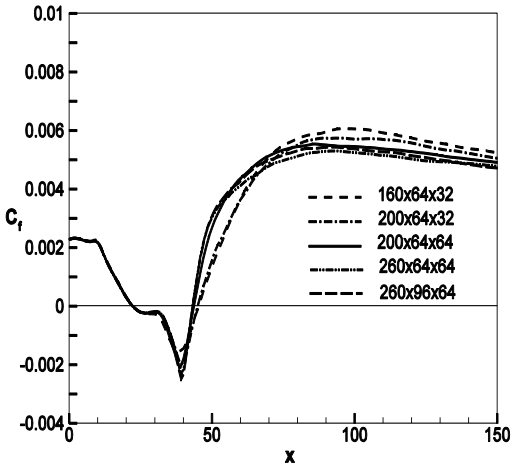

Fig. 3. Evolution of C_f for different grid levels.

It may be noted that being absolutely dissipative ,the Smagorinsky model is incapable of accounting for the backscatter and shows excessive dissipation. However, this shortcoming is partly offset by using the low-Reynolds number model of Voke (1996), which is expected to simulate the transitional flow.

Seven flow passes with wall disturbance were allowed to evolve the separation bubble, breakdown and the downstream development, each pass taking 10000 iterations. Statistics were taken for further ten flow passes after the flow reached dynamic stability. It may be noted that the dimensionless time step is 0.02. The simulation took about 70 hrs on an Intel Xeon, 2.6 GHz, quad-core, twin processor machine with 16 GB RAM.

3. RESULTS AND DISCUSSION

3.1 Validations

The LES solver used here has been thoroughly validated in several studies (Sarkar, 2007, 2008, 2009; Sarkar and Sarkar, 2009) for transitional and turbulent flows. As stated, the computational domain used here is same as that of Alam and Sandham (2000). It has also been confirmed that the normal and streamwise lengths were sufficient to resolve the developing boundary layer. However to check the spanwise length, the two-point correlations are calculated. In detail, turbulent flow consists of eddies in different size and orientation.

An idea of eddy size and orientation can be obtained by studying the relation between velocity and other fluctuating quantities at different locations and time. A correlation is defined as

$\overline{s_i s_j}\left(\bar{x},\bar{r},\tau\right)=\overline{s_i\left(\bar{x},t\right)s_j\left(\bar{x}+\bar{r},t+\tau\right)}$, where s_i, s_j are fluctuating quantities. Now, the space-time correlation coefficient is written as $R_{ij}=\dfrac{\overline{s_i s_j}\left(\bar{x},\bar{r},\tau\right)}{\sqrt{\overline{s_i^2}}\sqrt{\overline{s_j^2}}}$.

Two quantities are perfectly correlated if R = 1 and uncorrelated if R = 0. In general the value of R lies between 0 and 1. Following the above definition, the spanwise two-point correlations for different components of velocity are obtained as

$R_{uu}=\dfrac{\overline{u(z,t)u(z+dz,\tau)}}{\overline{u^2}}$, $R_{vv}=\dfrac{\overline{v(z,t)v(z+dz,\tau)}}{\overline{v^2}}$ and

$R_{ww}=\dfrac{\overline{w(z,t)w(z+dz,\tau)}}{\overline{w^2}}$

R_{uu}, R_{vv} and R_{ww} have been plotted in the Figs. 4(a), (b) and (c) respectively for different wall normal locations. In all these cases, the streamwise location is x = 150. The decay of the correlations to zero confirms that the domain length used in the spanwise direction is adequate.

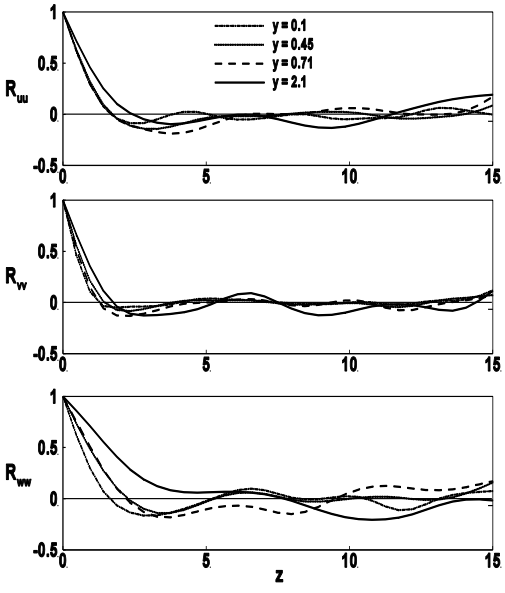

Fig. 4. Spanwise two-point correlations.

Figure 5 shows the evolution of C_f for different SGS models and comparison with the data of Alam and Sandham (2000). For calculating C_f , the local free-stream velocity given by $U_e(x,y)=-\int_0^y \omega_z dy$ (Spalart & Strelets, 1997) is used.

Table 4 Points of separation and reattachment for different simulations

Case		Separation Point (x/δ_{in}^*)	Reattachment Point (x/δ_{in}^*)	Point of $c_{f,min}$
Smagorinsky	C_s = 0.1	22.7	45.3	41.0
	C_s = 0.17	23.3	51.5	45.0
Dynamic model		22.3	43.6	39.0

Table 4 tabulates the mean separation and reattachment points. It is seen from C_f plots in Fig. 5 that results from the dynamic model are closer to the DNS of Alam and Sandham (2000).

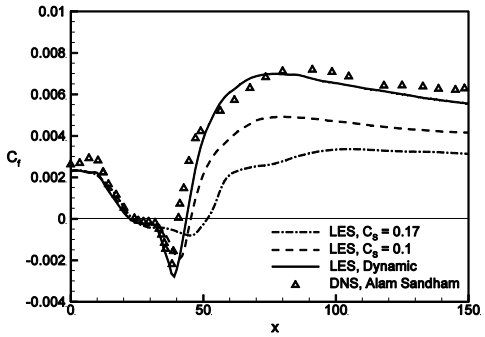

Fig. 5. Comparison of evolution of C_f for SGS models with DNS of Alam and Sandham (2000).

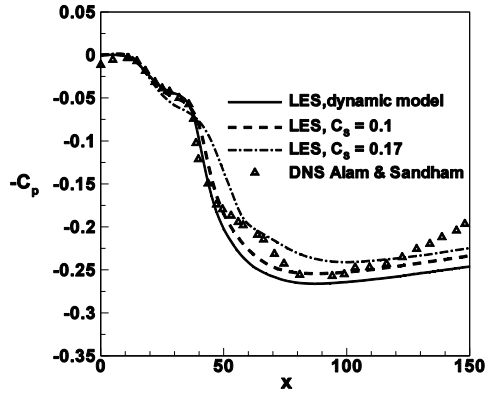

Fig. 6. Comparison of C_p for SGS models with DNS of Alam and Sandham (2000).

Smagorinsky model with C_s = 0.17 grossly overestimates the reattachment point and the bubble length. However, the reattachment point and bubble length predicted by the Smagorinsky model with a reduced value of model coefficient (C_s = 0.1) are very close to the values obtained from the dynamic model. After reattachment, the levels of C_f resolved by the Smagorinsky model under predict the DNS data.

Figure 6 shows the variation of normalized wall pressure along the streamwise direction for different sub-grid models. The distribution of pressure coefficient from the DNS of Alam and Sandham (2000) is also superimposed. The flow encounters an adverse pressure gradient after x = 15, depicting a negative slope of $-C_p$ curve. A sharp decrease in the value of C_p makes it clear that the bubble is of 'short' type. A slow favorable pressure gradient is observed downstream of reattachment indicating relaxation of boundary layer. The pressure distribution predicted by all the sub-grid models almost collapse on a single line and agree well with the DNS before the reattachment The differences are apparent downstream of reattachment, where, the flow resolved by the Smagorinsky model with reduced model coefficient approaches that of the dynamic model.

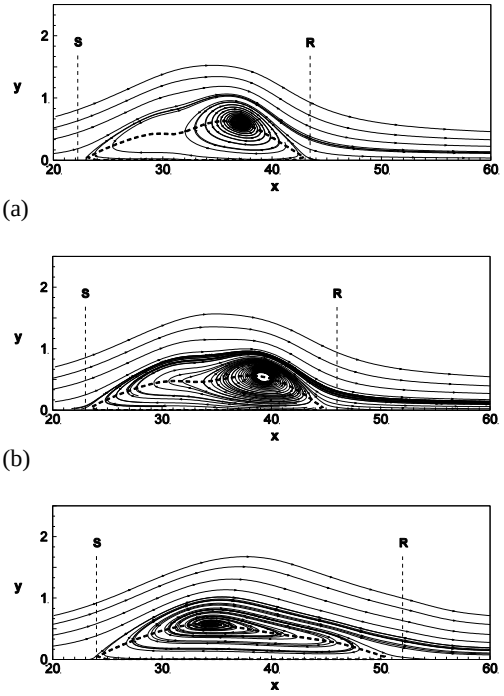

Fig. 7. LES of a laminar separation bubble showing streamlines and u_m= 0 line (dashed line) for (a) dynamic model; (b) Smagorinsky model, Cs = 0.1 and (c) Smagorinsky model, Cs = 0.17.

3.2 Mean Flow Structure

$Re_{\theta s}$ and Re_{lt} are two important variables used to characterize the mean flow. The length of transition (tl/δ_{in}^*) is defined as the distance from separation point to the point of minimum skin friction. The length of separation bubble (l_b/δ_{in}^*) is also calculated from C_f distributions for both the Smagorinsky and dynamic models.

The values of these parameters are tabulated and compared with the data of Alam and Sandham (2000) in Table 5. LES tends to predict larger bubble length and thus overestimate Re_{lt} particularly for the Smagorinsky model. The momentum thickness at separation θ_s is estimated as 0.533 against the DNS data of 0.49, whereas, Re_{θ_s}

Table 5 Data related to mean bubble shape

Case	l_b/δ^*_{in}	θ_s/δ^*_{in}	Re_{θ_s}	tl/δ^*_{in}	Re_{lt}
DNS, Alam & Sandham	16.4	0.49	246	-	6667
Dynamic model	21.3	0.533	266.5	16.7	7348
Smagorinsky, C_s=0.1	22.6	0.531	265.5	18.32	8060
Smagorinsky, C_s=0.17	28.2	0.530	265	21.71	9552

predicted by the LES is 266.5 against 246. All the SGS models evolve almost the same values of θ_s and Re_{θ_s}, difference in the values arising only at third decimal place.

Figure 7 shows the streamlines for all the LES cases, depicting the shape of the bubble and the recirculation region. The point of separation is marked as *S* and reattachment as *R*. The pictorial views of the bubbles from the Smagorinsky model with C_s= 0.1 and the dynamic model are more or less the same; however, the bubble from the Smagorinsky model with C_s= 0.17 looks very different with a large separation length. The length of the bubble progressively increases from the dynamic to Smagorinsky model with C_s= 0.17, where core of the recirculation is different for the three cases.

Figure 8(a) shows the mean streamwise velocity and Figs. 8(b)-(d) depict the root mean square streamwise, wall-normal and spanwise velocities respectively, obtained from the dynamic model. In Fig. 8(a) it is seen that the boundary layer develops against an adverse pressure gradient and separates near x = 22. The separation bubble with a flow reversal and the reattachment are also illustrated. The slow relaxation of the separated shear layer after reattachment, is also seen in Fig. 8(a). The evolution of turbulence after separation is demonstrated by Figs. 8(b)-(d). It is seen that the growth of perturbations starts just downstream of separation. The growth rate, after initial low, increases appreciably after x = 39, the location where C_f has the minimum value. This observation can be used to infer that turbulence is generated mainly in the reverse flow region. Fig. 9 demonstrates the growth of three-dimensional motion over the separation region using superimposition of streamlines and u_{rms} values. It clearly reflects that growth of u_{rms} occurs in the second half of the bubble, which becomes maximum near reattachment. The near wall turbulence appears several bubble lengths after reattachment.

Integral parameters such as δ^*, θ and shape factor ($H = \delta^*/\theta$) are important to characterize the shear layer. These are presented in Fig. 10. It is observed that the variations of δ^*, θ and H obtained from the dynamic model and the Smagorinsky model with C_s = 0.1 along with the correction for transition are almost identical. Thus, it demonstrates the usefulness of the modified Smagorinsky model for predicting transition of a separated layer. As expected, the results from the Smagorinsky model with C_s = 0.17 are not quite in agreement with the other two models and it is not recommended for this class of problems.

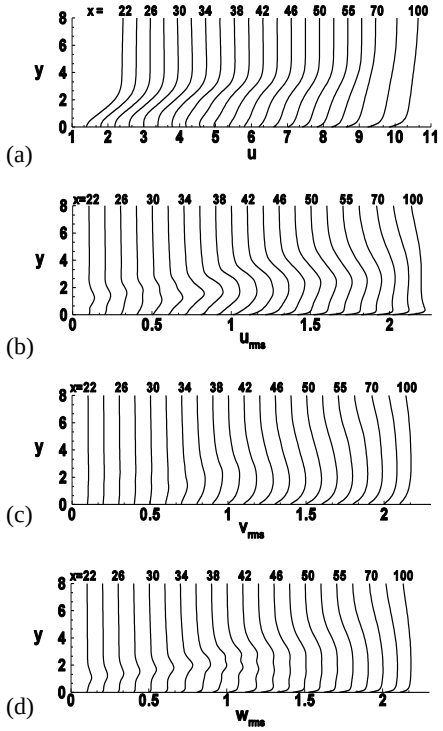

Fig. 8. Profiles of (a) u_m (b) u_{rms} (c) v_{rms} and (d) w_{rms}.

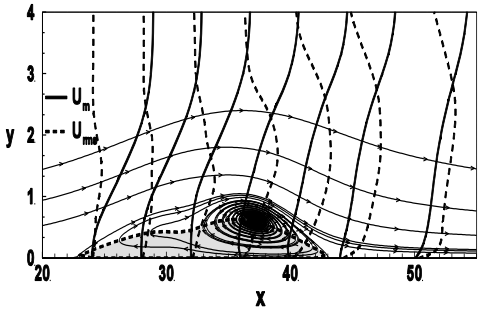

Fig. 9. LES of a laminar separation bubble showing streamlines, u_m and u_{rms} .

It is seen that δ^* increases from onset of separation, becomes maximum near the reattachment and decreases thereafter, whereas, θ drops a bit in the dead air region followed by a rapid increase in second-half of the bubble and then becomes asymptotic illustrating augmentation of turbulence with a slow relaxation after reattachment resulting in the maximum value of H near the point of minimum C_f, defined as the end of transition (x= 39), and the maximum value of H becomes 4.7. The value of shape factor at reattachment is 3.3, which agrees well with Horton's value, 3.5. Far downstream, this value drops down to approximately 1.5, indicating approach to equilibrium.

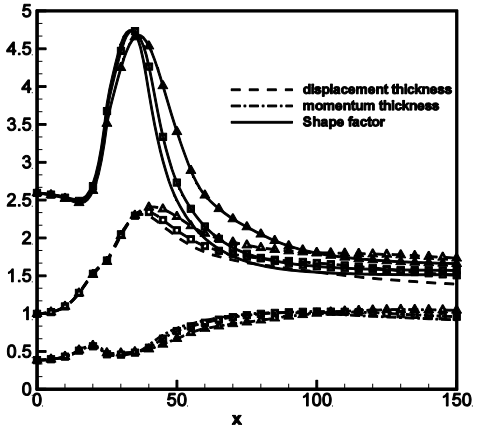

Fig. 10. Evolutions of δ^*, θ and H for the three SGS models. No symbol: dynamic model; □: Smagorinsky with C_s = 0.1; Δ: Smagorinsky with C_s= 0.17.

3.3 Transition and Three-dimensional Motions

Figure 11(a) shows contours of streamwise velocity in x-y plane at a particular time instant for the dynamic model. It shows that the shear layer thickens over the bubble, rolls up creating large-scale vortices, in typical K-H instability way. These vortices travel, retaining their structures, far downstream. This leads to predominant outer layer activities and slow relaxation to equilibrium. It may be noted that the darkest gray-scale represents the separation region and the separation is seen to extend to even around x = 60 as compared to the mean reattachment at x = 43.6 (Fig. 7(a)).

The top view (x-z plane) of streamwise velocity contours for y = 0.1 is shown in Fig. 11(b). The top-view confirms the initial two-dimensional character of the flow and the laminar separation of the boundary layer. The imposed perturbations seem to be growing with appearance of a sinuous spanwise undulation and the separated layer remains laminar up to x = 30. Three-dimensionality appears downstream of x = 35 and breakdown occurs near x = 43. The development of low-speed longitudinal streaks, characterizing near-wall turbulent flow, appears downstream of reattachment and is visible far downstream.

The side views (y-z plane) are shown in Fig. 11(c). The contours at x = 31.0 elucidate the two-dimensionality of the flow, though the spanwise symmetry about z = 0.38 L_z is slightly distorted due to transitional shear layer. The two-dimensionality is further disturbed at x = 39 with appearance of large-scale spanwise vortices. These vortices eject fluid from the inner layer and promote mixing. The initial symmetry is completely destroyed downstream of x = 83 and the near-wall fine-scale structures are apparent.

To elucidate further, amplification of disturbances in the x direction are shown in Fig. 12 for the dynamic model. The growth rate $d(\log u')/dx$ just after separation is 1.4 that increases to 6.2 in the middle of the bubble and then becomes 1.3 in the region around x/l = 0.7, followed by a slowdown before reattachment. Spalart and Strelets (2000) reported a growth rate of 1-4 in the transition region that subsequently goes downs to 2. The growth rates of w' at corresponding locations are 2.3, 7.1 and about 1.0. The value of u' approaches around 12% downstream, while v' and w' relax more slowly dropping to about 5.5% and 6.5% respectively.

Iso-surfaces of the spanwise component of instantaneous vorticity $\omega_z = \frac{\partial v}{\partial x} - \frac{\partial u}{\partial y}$ resolved by the dynamic model are presented in Fig. 13, which is very helpful to visualize the three-dimensional flow structure. The separated shear layer, which is two-dimensional initially, is distorted by nonlinear interactions and Λ-vortices appear in the transition region due to vortex stretching mechanism. Breakdown to small-scale and random structures with complete loss of orientation occurs just downstream of reattachment. The presence of longitudinal streaks is also evident after reattachment, which is the characteristic of turbulent layer. The present simulation is very consistent with the DNS of Alam & Sandham (2000) in resolving the flow structure. However, in their DNS, Spalart and Strelets (2000) did not observe Λ-vortices.

3.4 Turbulence Statistics

The contours of Reynolds stresses for the dynamic model are presented in Fig. 14 while the contours of turbulent kinetic energy (TKE) and the production (PKE) are depicted in Figs. 15 and 16 respectively. The imposed disturbances at x = 10 are reflected in contours of $\overline{u'u'}$, $\overline{w'w'}$ and TKE. These perturbations initially decay and then are amplified downstream. Reynolds stresses grow from x = 29, which is about 35% of the bubble length. A similar trend is observed for TKE and PKE contours. Thus stresses and TKE and PKE concentrate along the shear layer, moving away from the wall and showing their maxima near reattachment. In detail, $\overline{u'u'}$ is maximum at the reattachment (x = 43), whereas, the shear stress $\overline{u'v'}$ reaches the maximum just downstream of reattachment (x = 51). It takes

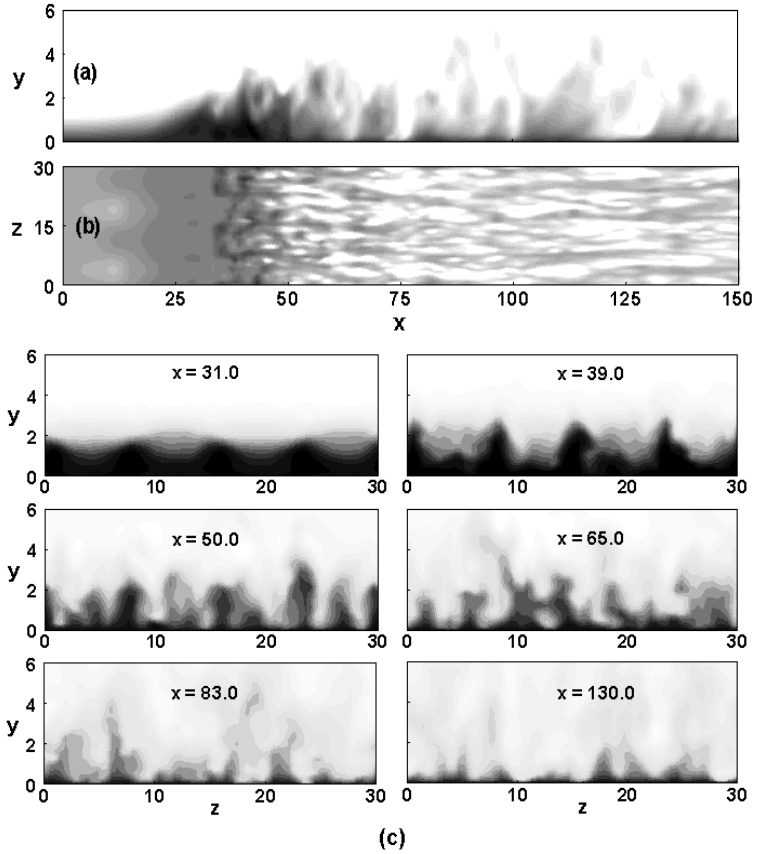

Fig. 11. Contours of instantaneous streamwise velocity: (a) *x*-*y* plane at *z* = 30.0; (b) *x*-*z* plane at *y* = 0.05; (c) *y*-*z* planes at indicated *x*-locations. Maximum level is 0.98 and minimum level is -0.13.

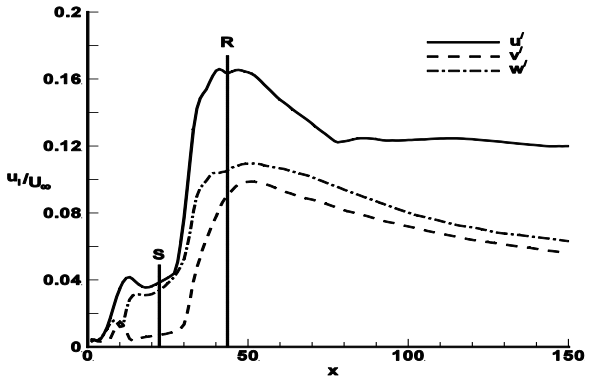

Fig. 12. Amplification of maximum r.m.s. values of u', v' and w' along the streamwise direction.

about 2.2 bubble lengths downstream for steep gradients of $\overline{u'u'}$ and $\overline{u'v'}$ to appear near to the wall. The contours of stresses, TKE and PKE are almost similar for the Smagorinsky model with low Reynolds number correction. However, the Smagorinsky model with C_s = 0.17 predicts a different evolution of stresses, TKE and PKE contours where the locations of their maxima change.

3.5 Boundary-layer Relaxation

Velocity profiles obtained from the dynamic model are shown in Fig. 17 for several downstream locations. It is observed that for the dynamic model, even at far downstream locations the profiles do not approach the universal logarithmic law of the wall and all profiles lie below the log-law. This has been observed by several researchers in experiments and simulations involving turbulent reattachment. Spalart and Strelets (2000) and Wasistho (1998) observed this in their simulations of laminar separation bubble. In their DNS, Le *et al.* (1997) noted this shift and gave a value of 2.54 for the intercept of logarithmic profile. They attributed this deviation to the combined effect of the low Reynolds number and adverse pressure gradient. In their experiments, Castro and Epik (1996) observed a similar effect.

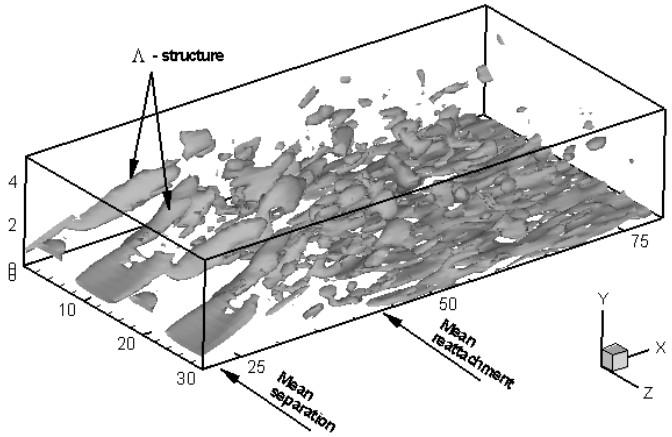

Fig. 13. Iso-surfaces of the spanwise component of instantaneous vorticity. Contour level is -0.55.

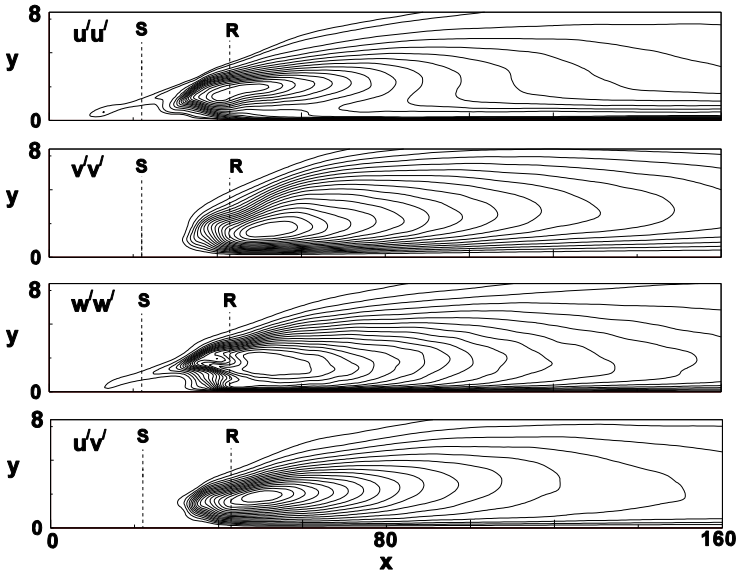

Fig. 14. Contours of $\overline{u'u'}$, $\overline{v'v'}$, $\overline{w'w'}$ and $\overline{u'v'}$; maximum contour levels are 0.0276, 0.0091, 0.0113 and 3.92×10^{-5} respectively.

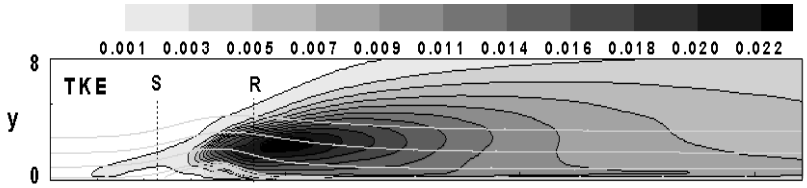

Fig. 15. Contours of TKE.

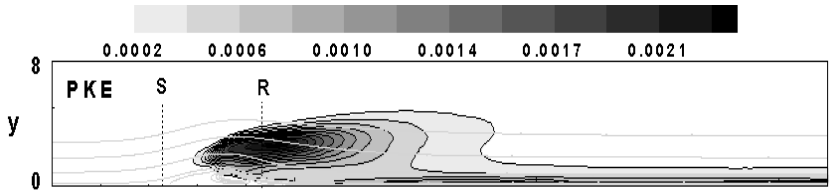

Fig. 16. Contours of PKE.

Departure of boundary layer from equilibrium can be measured by Clauser parameter, defined as $G = \frac{(H-1)}{H}\sqrt{2/C_f}$. For a flat plate boundary layer with zero pressure gradient, its equilibrium value is 6.8. However, in the presence of a weak favourable pressure gradient at low Reynolds number, this value may not be appropriate (Alam and Sandham, 2000). In Fig. 18, G is plotted against $(x-x_R)/\delta_R$, showing a comparison with the data available in the literature. The value of G which is initially very high, signifying a non-equilibrium layer, gradually decreases to 6.4 for the dynamic model. To reach equilibrium, Castro and Epik (1996) suggest a recovery length of at least $75\,\delta_R$.

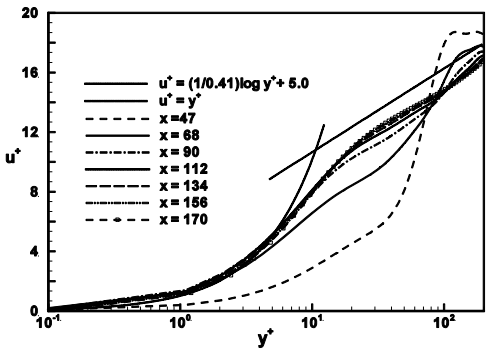

Fig. 17. Streamwise velocity profiles of relaxing boundary-layer for the dynamic model.

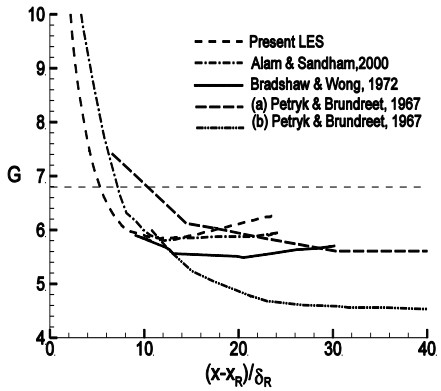

Fig. 18. Clauser parameter, δ_R/h = 5.8 (a), 3.47 (b), (Alam and Sandham, 2000).

In Fig. 19 the distance from reattachment to the peak of skin friction (l_r) normalized by bubble length has been plotted as a function of bubble length normalized by momentum thickness at separation.

Data from the present study has been compared with the data from Spalart and Strelets (1997), Wasistho (1998) and a correlation (Alam and Sandham, 2000) given by

$$\frac{l_r}{l_b} = \frac{1}{2.4 - 69\left(\theta_s / l_b\right)} \qquad (6)$$

It can be seen from the plot that the data from the Smagorinsky model model with C_s = 0.1 and the dynamic model are very close to the solid line representing the correlation given by Eq. (6) while Smagorinsky model with C_s = 0.17 does not seem to follow it.

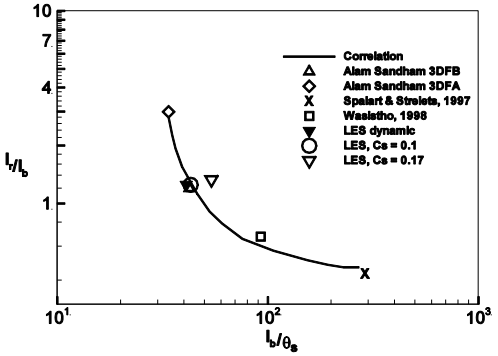

Fig. 19. Bubble length versus the recovery length.

4. CONCLUSIONS

The present LES with dynamic model produces encouraging results, illustrating instability of shear layer, its transition and then breakdown leading to reattachment. It is demonstrated that the standard Smagorinsky model being too dissipative, fails to properly resolve transition of the separated layer. It, however, shows a close agreement with the dynamic model when it is modified and a reduced model constant is applied. Although, there are some differences in minute detail, it is worthwhile to use the low-Reynolds number correction for the class of problems involving shear layer transition.

Comparison of various parameters and three-dimensional visualization of instantaneous flow fields indicate that the dynamic model gives the most physically accurate description of transition. LES using the dynamic model closely reproduces the results of Alam and Sandham (2000) in the description of quantities of interest such as the point of separation, length of the separation bubble, momentum thickness at separation etc. The differences can be attributed to several factors including but not limited to imprecise definition of boundary-layer quantities.

The simulations reveal that in the first quarter of bubble length the rate of growth of fluctuations is very small. Breakdown to turbulence takes place in the last half of the bubble. Turbulence statistics confirm the dominance of turbulent activities in the last half of the bubble and near reattachment. The development of near wall characteristics takes place far downstream. It is observed that the velocity profiles do not attain the universal log-law even far downstream; the value of intercept being 3.5. This observation is confirmed by the findings of other researchers too.

Thus, it can be concluded that LES adequately resolves the flow field and transition. A DNS will reveal more features, but at a significant increase in

the computational cost.

REFERENCES

Alam, M. and N. D. Sandham (2000). Direct numerical simulation of 'short' laminar separation bubbles with turbulent reattachment. *Journal of Fluid Mechanics* 403, 223–250.

Allen, T. and N. Riley (1995). Absolute and convective instabilities in separation bubbles. *The Aeronautical Journal* 99, 439-448.

Brinkerhoff, J. R. and M. I. Yaras (2011). Interaction of viscous and inviscid instability modes in separation-bubble transition. *Physics of Fluids* 23, 124102

Castro, I. P. and E. Epik (1996). Boundary layer relaxation after a separation region. *Experimental Thermal and Fluid Science* 13, 338-348.

Dovgal, A. V., V. V. Kozlov and A. Michalke (1994). Laminar boundary layer separation: Instability and associated phenomena. *Progress in Aerospace Sciences* 30, 61-94.

Gaster, M. (1967). The structure and behaviour of separation bubbles. *Aeronautical Research Council* R & M 3595.

Germano, M., U. Piomelli, P. Moin and W. H. Cabot (1991). A dynamic subgrid-scale eddy viscosity model. *Physics of Fluids A* 3, 1760-1765.

Horton, H. P. (1967). A semi-empirical theory for the growth and bursting of laminar separation bubbles. *Aeronautical Research Council*.

Jones, L. E., R. D. Sandberg and N. D. Sandham (2010). Stability and receptivity characteristics of a laminar separation bubble on an aerofoil. *Journal of Fluid Mech*anics 648, 257-296.

Kim, J., P. Moin and R. Moser (1987). Turbulent statistics in fully developed channel flow at low Reynolds number. *Journal of Fluid Mechanics* 177, 133-166.

Le, H., P. Moin and J. Kim (1997). Direct numerical simulation of turbulent flow over a backward facing step. *Journal of Fluid Mecanics* 330, 349-374.

Lilly, D. K. (1992). A proposed modification of the Germano subgrid-scale closure method. *Physics of Fluids A* 4, 633-635.

Lin, J. C. and L. L. Pauley (1996). Low-Reynolds-number separation on an airfoil. *AIAA Journal* 34(8), 1570-1577.

Marxen, O. and U. Rist (2010). Mean flow deformation in a laminar separation bubble. *Journal of Fluid Mechanics* 660, 37–54.

Marxen, O., M. Lang, U. Rist and S. Wagner (2003). A combined experimental/ numerical study of unsteady phenomena in a laminar separation bubble. *Flow, Turbulence and Combustion* 71, 133–146.

McAuliffe, B. R. and M. I. Yaras (2008). Numerical study of transition mechanisms leading to transition in separation bubbles. *ASME Journal of Turbomachinery* 130(2), 021006.

Orlanski, I. (1976). Simple boundary condition for unbounded hyperbolic flows. *Journal of Computational Phys*ics 21, 251-269.

Ovchinnikov, V., U. Piomelli and M. M. Choudhari (2006). Numerical simulations of boundary-layer transition induced by a cylinder wake. *Journal of Fluid Mechanics* 547, 413-441.

Pauley, L. L., P. Moin and W. C. Reynolds (1990). The structure of two-dimensional separation. *Journal of Fluid Mechanics* 220, 397-412.

Ripley, M. D. and L. L. Pauley (1993). The unsteady structure of two-dimensional steady laminar separation. *Physics of Fluids A* 5(12), 3099-3106.

Roberts, S. K. and M. I. Yaras (2006). Large eddy simulation of transition in a separation bubble. *ASMS Journal of Fluids Engineering* 128, 232-238.

Roberts, W. B. (1980). Calculation of laminar separation bubbles and their effect of airfoil performance. *AIAA Journal* 18, 25-31.

Sarkar, S. (2007). The effects of passing wakes on a separating boundary layer along a low-pressure turbine blade through large-eddy simulation. *IMechE Journal of Power and Energy* 221, 551-564.

Sarkar, S. (2008). Identification of flow structures on a LP turbine blade due to periodic passing wakes. *ASME Journal of Fluids Engineering* 130(6), 061103.

Sarkar, S. (2009). Influence of wake structure on unsteady flow in an LP turbine blade passage. *ASME Journal of Turbomachinery* 131(4), 041016.

Sarkar, S. and S. Sarkar (2009). Large-Eddy Simulation of Wake and Boundary Layer Interactions Behind a Circular Cylinder. *ASME Journal of Fluids Engineering* 131(9), 091201.

Smagorinsky, J. (1963). General circulation experiments with the primitive equations. I: The basic experiment. *Monthly Weather Review* 1991(3), 99-165.

Spalart, P. R. (1988). Direct simulation of turbulent boundary layer up to Reθ = 1410. *Journal of Fluid Mechanics* 187, 61 -98.

Spalart, P. R. and M. K. Strelets (1997). Direct and Reynolds-averaged numerical simulation of a transitional separation bubble. *11thsymposium on Turbulent shear Flows*, Grenoble , France.

Spalart, P. R. and M. K. Strelets (2000). Mechanisms of transition and heat transfer in a separation bubble. *Journal of Fluid Mechanics* 403, 329–49.

Voke, P. R. (1996). Subgrid-scale modeling at low mesh Reynolds number. *Theoretical and Computational Fluid Dynamics* 8, 131-143.

Wasistho, B. (1998). *Spatial direct numerical simulation of compressible boundary layer flow*. Thesis, University Twente, Enschede, The Netherlands.

Wissink, J. G. and W. Rodi (2003). DNS of a laminar separation bubble in the presence of oscillating external flow. *Flow, Turbulence and Combustion* 71, 311-331.

Yang, Z. Y. and P. R. Voke (2001). Large eddy simulation of boundary layer separation and transition at change of surface curvature.*Journal of Fluid Mechanics* 439, 305-333.